© 2006 The Chemical Society of Japan

Selected Paper

High-Pressure ^{129}Xe NMR Study of the Intermolecular Interaction of Xenon Confined in Activated Carbon Fiber (ACF)

Takahiro Ueda,*[1,2] Hironori Omi,[1] Takanori Yukioka,[1] and Taro Eguchi[1,2]

[1]The Museum of Osaka University, Osaka University, 1-1 Machikaneyama, Toyonaka, Osaka 560-0043

[2]Department of Chemistry, Graduate School of Science, Osaka University, 1-1 Machikaneyama, Toyonaka, Osaka 560-0043

Received June 3, 2005; E-mail: ueda@museum.osaka-u.ac.jp

The pressure dependence of a ^{129}Xe chemical shift (δ) and the local density of xenon adsorbed in activated carbon fiber (ACF) with slit-pore widths of 0.7–1.1 nm was investigated using in-situ high-pressure ^{129}Xe NMR. ^{129}Xe chemical shift values below 0.025 MPa change linearly with equilibrium pressure. The initial slope of the pressure dependence of δ led to a shift value at zero pressure, δ_S', which approximately reflects the xenon–wall interaction. A statistical model incorporating the xenon–wall interaction well interprets the dependence of δ_S' on the pore width. Furthermore, in a higher-pressure region, the density dependence of the chemical shift led to the xenon–xenon interaction via the virial coefficients of the chemical shift up to the second order on density (the third-virial coefficient). The second-virial coefficient (a coefficient for the linear term of density) depended on the pore width. Increasing the slit width from 0.7 to 1.1 nm increased the second-virial coefficient, δ_1, from 42×10^{-3} to 78×10^{-3} ppm kg^{-1} m^3, suggesting that the space accessible by the surrounding xenon atoms increases when the slit width increases. This aspect reveals the size effect of the xenon–xenon interaction in nanospace.

Xenon-129 NMR spectroscopy is an excellent medium to study the structure and porosity of porous materials.[1–5] The possibility of using Xenon-129 as a probe for the inner space of materials was proposed by Ito and Fraissard[6] in 1980, who first applied ^{129}Xe NMR to study the interaction between xenon and surfaces in some zeolites. They found a correlation between ^{129}Xe chemical shift values and pore size. Almost concurrently, ^{129}Xe NMR was applied by Ripmeester and Davidson to study the size and shape of the local structure of xenon in clathrate compounds, including xenon.[7] Since the pioneering study, ^{129}Xe NMR spectroscopy has been applied to study the local structures of myriad materials: zeolites,[5,8] glasses,[9] fullerenes,[10] carbon nanotubes,[11] polymers,[12–15] clathrate compounds,[16–19] liquid crystals,[20–22] some organic solvents,[4,23] and proteins in solution.[23–25]

In ^{129}Xe NMR for xenon adsorbed in porous media under low-loading conditions where the linear relationship is held between density and pressure, the ^{129}Xe chemical shift value (δ) is represented by the sum of several terms corresponding to various perturbations as[5]

$$\delta = \delta_0 + \delta_S + \delta_{Xe} + \delta_{SAS} + \delta_E + \delta_M, \quad (1)$$

where δ_0 is the reference (xenon gas at zero density) and δ_S arises from interactions between xenon and the surface without specific electric or magnetic interactions. It depends only on the dimensions of the cages or channels. The contribution of xenon–xenon interaction is δ_{Xe}, which is given approximately as $\delta_{Xe\text{–}Xe}\rho_{Xe}$. Although the xenon–xenon as well as xenon–wall interactions may contribute to the density dependence of δ, the xenon–xenon binary interaction dominantly contributes to $\delta_{Xe\text{–}Xe}$. This assumption is verified in many zeolite systems.[5] In the high-loading region, the non-linear terms on the density is added to this term, which includes the xenon–xenon ternary interactions as well as the xenon–wall interaction perturbed by the reduction of the free volume under the high-loading of xenon. For strong adsorption sites (SAS) in the void space interacting with xenon, δ_{SAS} contributes to δ at a very low level of xenon loading. Furthermore, when SAS sites have large electric charges (e.g., divalent and trivalent cations such as Mg^{2+}, Ca^{2+}, La^{3+}, and Y^{3+}) or occasional paramagnetic cations (e.g., paramagnetic transition metals such as Co^{2+}, Ni^{2+}, etc.), δ_E and δ_M are also added, which are respective effects of electric and magnetic fields on the chemical shift values. For the loading dependence of δ, the shift value at the zero density thereby reflects the pore size through Xe–wall interaction,[26,27] whereas the shift value in the high-loading region depends on the local density of xenon that is adsorbed in the pores, providing the xenon–xenon interaction.[15,28–31]

In the bulk xenon, the high-pressure condition causes a phase transition to a supercritical fluid, which is very useful in a variety of fields, e.g. analytical chemistry,[82] synthesis,[83] and catalysis.[84] Thus, the supercritical phenomenon has attached intense interest of a great deal of researchers. A number of studies on supercritical fluids have been performed using spectroscopic methods such as infrared, Raman, small angle X-ray or neutron scattering, and NMR.[78–81] The xenon–xenon interaction through the density dependence of the ^{129}Xe chemical shift is expected to be a useful index to understand microscopic features in the supercritical fluid. Recently, Brunner et al. have developed a high-pressure cell made from a sapphire tube. Using it, they have measured the ^{129}Xe chemical shift value in bulk xenon gas and supercritical fluid up to about

Published on the web February 10, 2006; DOI 10.1246/bcsj.79.237

70 MPa.[36] However, detailed analysis on the density dependence of δ and the following discussion relating to the intermolecular interaction in the supercritical fluid have not yet been done.

In this context, our growing interest exists in supercritical phenomenon of xenon in the nanospace. A nanometer-sized space fulfils the intermediate environments between the bulk and an isolated molecule, leading to molecular assembly being scaled to the mesoscopic size. Understanding of the physicochemical properties of xenon in the mesoscopic space will open an interesting avenue to the fascinating, fundamental, and unprecedented research field and its applications to supercritical fluids. In order to understand the aggregation of xenon in the nanospace from the microscopic point of view, we are interested in the local structure and dynamics of xenon in nanospace as well as the size effect for the xenon–xenon and the xenon–wall interactions.

Recently, we have developed a conventional in-situ variable-pressure NMR probe that allows studies with pressures as great as 20 MPa.[15] We have applied the probe to study: xenon–wall interaction in the free volume of polymers,[32] the intermolecular interaction of xenon confined in 1D-nanochannels,[28,33] supercritical phenomena of xenon in the mesoporous silica,[34] and the local structure of xenon confined in some zeolites.[35]

The present study examines the pressure and fluid density dependence of the ^{129}Xe chemical shift value of xenon adsorbed in activated carbon fibers (ACFs). Activated carbon is a traditional adsorbent material that has been used extensively in industrial, catalytic, biological, and environmental applications. Traditional activated carbons are amorphous. Therefore, structural characterization of the surface and pores is complex. Recently, developed carbon materials, ACFs, comprise highly ordered organic fibers and interstices of the micro-graphite seats that form uniform and slit-type micropores.[37–39] Local structures of adsorbates in ACF micropores have been studied for many molecules: He,[40–42] Xe,[43] NO,[44] H_2O,[45–47] ethanol,[48] CCl_4,[49,50] benzene,[51] O_2,[52–54] and SO_2.[55] Recently, the molecular self-assembly and formation of an ordered structure of adsorbates in ACF have been of great interest, with xenon attracting particular attention. Xenon has a large van der Waals diameter (0.432 nm) and large polarizability volume (4.04×10^{-30} m^3). Therefore, it interacts strongly with other xenon molecules as well as the wall surface of pores. This strong interaction is expected to result in specific and interesting structures around the adsorbed xenon such as xenon clustering. In addition, nanometer-sized space is also anticipated to elicit the size effect of intermolecular interaction of xenon confined in the pore. Thus, we are confident that the microscopic behavior of xenon confined in the ACF micropore provides a fruitful and comprehensive clue to understand the supercritical phenomenon in nanospace.

Therefore, we have applied an in-situ high-pressure ^{129}Xe NMR technique to investigate the xenon–wall as well as xenon–xenon interaction of adsorbed xenon in ACF micropores. Using ^{129}Xe chemical shift values at zero pressure, we discuss the dependence of δ_S on the pore width. Furthermore, to evaluate δ_{Xe}, the pressure dependence of the ^{129}Xe chemical shift value of xenon adsorbed in ACF micropores has been represented as a function of fluid density by xenon adsorption isotherms, and analyzed using the virial expansion of the chemical shift by fluid density. Xenon–xenon intermolecular interaction in nanospace is discussed based on the second-virial coefficient of the chemical shift.

Table 1. Characterization of Micropores for ACF Determined by N_2 Isotherm

Sample	W_0 /10^{-6} m^3 g^{-1}	A_{ext} /m^2 g^{-1}	A_t /m^2 g^{-1}	w /nm
10A	0.37 ± 0.01	18 ± 5	1100 ± 100	0.7 ± 0.1
15A	0.58 ± 0.01	21 ± 8	1410 ± 30	0.83 ± 0.01
20A	0.90 ± 0.02	59 ± 20	1690 ± 50	1.1 ± 0.1

Experimental

Pitch-based activated carbon fibers (ACF) with different pore widths were supplied by Osaka Gas Co., Ltd., and are denoted respectively as 10A, 15A, and 20A (the number denotes the crude pore size supported by the supplier, and the character "A" represents "ACF"). Characterization of ACF micropores was carried out with the N_2 adsorption isotherm at 77 K using a surface analyzer system (Gemini-2360; Shimadzu Corp.). Those data yielded the micropore volume (W_0), the specific surface area (A_{ext} and A_t), and the slit-pore width (w) by the subtracting pore-effect method,[56] as listed in Table 1.

In-situ ^{129}Xe NMR measurements were carried out using Bruker Model MSL-200 and DSX-200 pulsed spectrometers operating at a Larmor frequency of 55.6 MHz; a home-built pressure-variable NMR probe was installed.[15] Fibrous ACF samples were packed into a glass tube of 5 mmϕ, with one rounded end and the open end capped with glass wool. They were heated to 200 °C under reduced pressure (<2 Pa) for 24 h. Pretreated glass tubes containing samples were placed in a pressure-resistant NMR cell made of ZrO_2. The prepared NMR cell was then mounted on a high-pressure NMR probe. The ACF samples were evacuated for 2 h under reduced pressure (<1 kPa) before xenon gas was loaded into the sample cell. The FID signals were recorded in a single-pulse experiment with a pulse delay of 5 s, $\pi/2$-pulse of 3 μs and the accumulation of 8–8192, depending on the signal-to-noise ratio, over pressures of 0.001–5 MPa at 298 K. The ^{129}Xe chemical shift was referred by a signal from bulk xenon gas at zero density.[34] The ^{129}Xe chemical shift value between the different batch samples in each ACF, which were treated under similar conditions (evacuating at 200 °C for about 1–2 days), was reproduced over all of the pressure region within the experimental error of ±5 ppm. Temperature and pressure were controlled within an experimental error of ±0.5 K and 10% in MPa, respectively.

High-pressure xenon adsorption isotherms were measured using a high-sensitivity magnetic suspended gravimetric system (Rubotherm Präzisionsmesstechnik GmbH, Bochum, Germany). High-purity-grade xenon gas was purchased from Japan Air Gases Ltd. A known amount of ACF (ca. 0.2 g) was heated to 200 °C under reduced pressure (<2 Pa) for 24 h before mounting on a sample basket. The pretreated sample was mounted on a sample basket made from stainless steel. Before measurements, the system was evacuated at 5×10^{-1} Pa for one day. Adsorption isotherms were measured at 298 K in a pressure range of 0.01–5 MPa. The resolution of the weight measurements of the magnetic balance was within $\pm 10^{-5}$ g. Equilibrium weights were achieved for 40–60 min. The observed change in the sample weight, Δg, led to the absolute amount of adsorbates, a_{Xe}, according to the following relationship:[57]

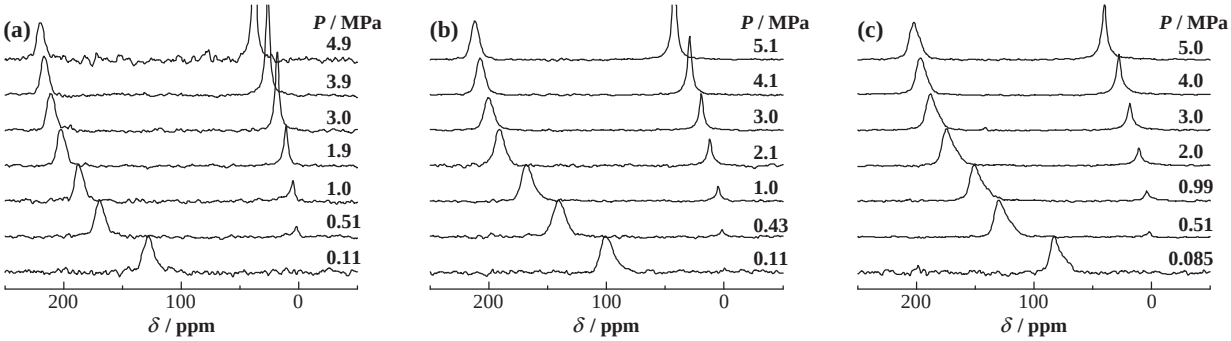

Fig. 1. Pressure dependence of ^{129}Xe NMR spectra of xenon confined in ACF micropores at 298 K for 10A ($w = 0.7$ nm) (a), 15A ($w = 0.83$ nm) (b), and 20A ($w = 1.1$ nm) (c).

$$\Delta g = ma_{Xe} - m(W_0 + 1/\rho_s)\rho - V_0\rho, \quad (2)$$

where m is the adsorbent sample mass, ρ and ρ_s represent the bulk xenon density and the pycnometric density of an adsorbent, respectively, W_0 is the pore volume, and V_0 is the volume of the sample holder. The resultant isotherms were analyzed using Dubinin–Radushkevich (DR) plotting.[58–60]

Results and Discussion

Pressure Dependence of ^{129}Xe Chemical Shift in ACFs. Figures 1a–1c show the pressure dependence of the ^{129}Xe NMR spectra of xenon in ACFs. Each spectrum consists of two peaks. The peak between 0 and 50 ppm is assigned to the free xenon gas that co-exists with the ACF sample, because the chemical shift value of this peak agrees with that in bulk xenon gas (vide infra). On the other hand, the peak between 80 and 220 ppm is assigned to xenon in the ACF sample. In general, there are four main sites in the microporous materials such as zeolites and activated carbons: outer- and inner-surface of the pore, the void space in the pore, and interparticle space. The dynamic averaging of xenon among these sites results in the observed signal. Even in ACFs, xenon occupying these sites is contributed to the resonance line. The observed signal depends on the inherent chemical shift value and the population of xenon in each site. At the first approximation, xenon on the outer- and inner-surface of the pore has similar values for the inherent shift, because xenon atoms interact directly with the ACF surface on both sites. Furthermore, xenon existing in both the void space of the micropore and the inter-fiber space will approximately give rise to a chemical shift value similar to that in bulk xenon gas. However, the fibrous ACF samples are expected to show an effective volume of inter-fiber space much smaller than the fine particle samples, leading to a small contribution of xenon in the inter-fiber to the observed signal. In addition, it is probable that xenon adsorbed on the outer-surface of the micropore contributes little to the observed signal because of the narrow external surface area, which is about 1.5–3.5% of the total surface area as listed in Table 1. Therefore, the observed peak in the chemical shift range from 80 to 220 ppm is mainly originated from the dynamic averaging of xenon between the inner-surface and void space in the ACF micropore.

Both peaks shift to the lower field side with increasing pressure. The peaks for xenon in ACF are broader than that for free xenon gas; they are also somewhat asymmetric. As the xenon loading (increase of pressure) increases, the line width narrows and the shape becomes symmetric, implying that xenon–xenon interaction plays a dominant role to symmetrize and narrow the resonance peak. Two major possibilities exist for peak modification; one is the powder pattern of chemical shift anisotropy, and another is inhomogeneity of magnetic susceptibility because of the fibrous shape of the samples. Line-shape simulation based on chemical-shift anisotropy cannot reproduce these asymmetric line shapes completely. In fact, our previous work showed that the ^{13}C resonance line of CO_2 adsorbed in ACF was broadened and asymmetric because of the inhomogeneity of the magnetic susceptibility of the fibrous sample.[77] However, its origin is independent of xenon loading. Taken together, the inhomogeneous adsorption sites on the pore wall of the ACF micropore might cause the inhomogeneous distribution of the chemical shift. Two sites for xenon exist in the micropore; one is on the pore wall and the other is in nanospace. Even in the ACF micropore, the pore surface structure has an inhomogeneous distribution, leading to inhomogeneous distribution of the chemical shift of xenon, which depends mainly on it. In contrast, xenon existing in the nanospace acts approximately as the free xenon gas, which gives rise to an isotropic and narrow resonance line. The observed signal results from the dynamic average of xenon between these sites as described above. In the low-loading region, the observed line strongly reflects the contribution from the former site, resulting in the broad and asymmetric peak. The contribution of the latter site increases simultaneously with the increase in xenon loading. Consequently, the observed peak narrows and becomes symmetric. The chemical shift value at the peak maximum is used herein for discussion.

Figure 2 shows the pressure dependence of the ^{129}Xe chemical shift value (δ) for each peak. The shift values of free xenon gas in three kinds of ACF mutually coincide throughout the pressure range. These values also agree with the shift value for bulk xenon gas observed with no adsorbents,[34] thereby indicating that the peak observed for free xenon gas originates from a co-existing gaseous component that has little contribution to the chemical exchange with confined xenon. For xenon confined in ACF micropores, the shift values increase markedly, even in the low-pressure region below 1.0 MPa. Xenon loading causes an increase in the local density of xenon in ACF micropores. For that reason, variation in δ is characterized mainly by δ_{Xe} in Eq. 1, which is proportional to the fluid density of xenon in the low-density region. In particular,

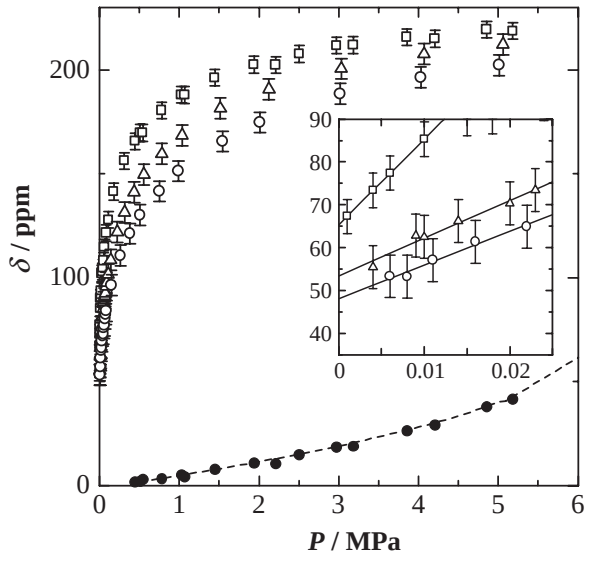

Fig. 2. Pressure dependence of ^{129}Xe chemical shift values at 298 K for xenon confined in ACF micropores; 10A ($w = 0.7$ nm) (□), 15A ($w = 0.83$ nm) (△), and 20A ($w = 1.1$ nm) (○). The shift values of free xenon gas (●) co-existing with the samples coincide among all three samples, and are in good agreement with the shift value (represented by a broken line) for bulk xenon gas with no adsorbents. The inset shows the expansion of the low-pressure region below 0.025 MPa, in which the chemical shift values in respective samples seem to obey Henry's law.

the rapid increase in δ below 1 MPa suggests that xenon adsorption in ACF micropores is dominantly characterized by a micropore-filling mechanism, where adsorption is accelerated at low pressure by the deeper potential emphasized by the pore walls. The increment of δ reaches 150 ppm with increasing pressure up to 5 MPa. The increment contains the shift value in the bulk supercritical fluid (160 ppm at 6.5 MPa), implying that xenon confined in ACF micropores experiences high pressure similar to that in the bulk supercritical fluid.

Xenon–Wall Interaction via δ_S. The inset of Fig. 2 shows the pressure dependence of a ^{129}Xe chemical shift below 2.5×10^{-2} MPa, where δ increases linearly with pressure. The observed chemical shift value may include the contribution of xenon adsorbed on the outer- and inner-surface of the ACF micropore. However, the narrow external surface area of ACF in comparison with the internal surface area and the micropore filling mechanism lead to this conceivable condition, i.e., the very small population of xenon on the outer-surface and the abundant adsorption of xenon in the micropore. Therefore, the contribution of xenon adsorbed on the outer-surface is assumed to be negligible in order to analyze the observed shift value.

Furthermore, the linearity of the pressure dependence of δ corroborates the additivity of the chemical shift value caused by the xenon–xenon binary interatomic interaction and the xenon–wall interaction perturbed by xenon loading. This result validates at the very least the additivity of the shift component in Eq. 1 up to the third term. Thus, Eq. 1 leads to Henry's law, $\delta = \delta_S' + K'P$, which is reasonable to describe the experimental result in this pressure region.

Table 2. ^{129}Xe Chemical Shift Value at Zero Density, the Coefficients of Henry's Law

Sample	δ_S' /ppm	K' /10^3 ppm MPa^{-1}
10A	65 ± 4	2.0 ± 0.1
15A	53 ± 5	0.9 ± 0.2
20A	48 ± 5	0.8 ± 0.2

The δ_S' value was determined for each specimen by extrapolating δ to zero pressure. At the limit of zero pressure, the chemical shift value is dominated only by the xenon–wall interaction. However, ACFs are known to contain paramagnetic spin resulting from a dangling bond. In the pitch-based ACF supplied by Osaka Gas Co., Ltd., the spin density was estimated as 5×10^{17} g^{-1}.[61] This spin density corresponds to a volume of 1000 nm^3 including spin. Since this concentration is low, it is reasonable that δ_S' is affected mainly by the xenon–wall interaction, but the local magnetic field caused by paramagnetic spin might contribute to δ_S' in the term δ_M. Table 2 lists the obtained δ_S' values for ACFs.

The δ_S' value increases with decreasing slit-pore width, implying that the smaller the pore width, the greater the Xe–wall interaction. The relationship between δ_S and the void space was initially examined in zeolites.[26,27] An early description of the relationship between δ_S and pore diameter was proposed by Demarquay and Fraissard.[27] They introduced the mean free path of xenon to describe the extent of free space in the cavity. On zeolites, the empirical relationship is represented as

$$\delta_S{}^{-1} = \frac{1}{243}\left(1 + \frac{\bar{l}}{0.2054}\right). \quad (3)$$

The mean free path of a xenon atom can be derived easily for cavities with a spherical or infinite-cylinder shape. The mean free path is given as $\bar{l} = (D_S - 0.44)/2$ for a spherical cavity and $\bar{l} = D_S - 0.44$ for an infinite cylinder when D_S denotes the cavity diameter. Figure 3 shows the plot of $\delta_S{}^{-1}$ against the pore width; Equation 3 gives lines for the infinite cylinder pore and the spherical pore, respectively. The observed $\delta_S'{}^{-1}$ values are larger than both expected values. This earlier treatment does not describe the relationship between δ_S' for confined xenon and pore width in ACF micropores.

On the other hand, Cheung reported the temperature dependence of the ^{129}Xe chemical shift in the infinite parallel layer.[62] In this model, the temperature dependence of δ_S is considered by integrating chemical shielding caused by xenon–wall interactions over the entire space between parallel layers:

$$\delta_S(T) = \frac{\int^V \delta(\mathbf{r}) \exp[-U(\mathbf{r})/kT]\mathrm{d}\mathbf{r}}{\int^V \exp[-U(\mathbf{r})/kT]\mathrm{d}\mathbf{r}}. \quad (4)$$

This equation represents the chemical shielding, σ, in Ref. 62 instead of the chemical shift, δ. In ^{129}Xe NMR, δ_S is equal to $-\sigma_S$. Interaction of the adsorbed xenon with a surface atom is modeled as a pairwise Lennard–Jones 6-12 potential, $u(r) = -4\varepsilon[(a/r)^6 - (a/r)^{12}]$, where ε is the depth of the potential well and a is the position of the zero potential energy. Because

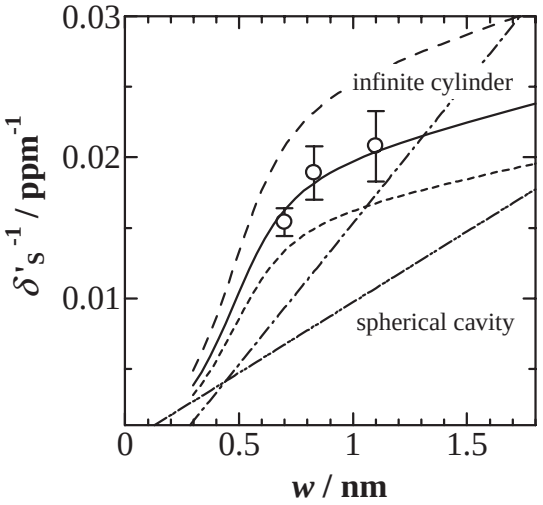

Fig. 3. A plot of the reciprocal value of $\delta_S{}'$ against the pore width, w, of ACFs. Linear lines show the expected values using Eq. 3 for infinite cylinder (dot-dashed line) and spherical cavities (dash-dot-dashed line), which empirically suggests an relationship between $\delta_S{}'$ and the mean free path of xenon in the void space. The solid curve shows the result of best fitting using Eqs. 4, 5, and 6 for the LJ parameter, $\varepsilon_{Xe\text{–}C}/k_B = 78\,K$ and $a_{Xe\text{–}C} = 0.375\,nm$, and $c = 0.046\,ppm\,K^{-1}$. The upper and lower curves represented by broken lines are calculated values using 0.036 ppm K^{-1} and 0.056 ppm K^{-1} for c, respectively.

the ACF wall is composed only of carbon atoms, we take account of the Lennard–Jones 6-12 potential between xenon and all of the surface carbon atoms as the total potential $U(r)$. For a xenon atom trapped between two infinite parallel carbon sheets with w separation, $U(r)$ is the sum of the pairwise 6-12 potentials over all surface atoms on both sheets. It is a function of the xenon–wall distance, r $(-w/2 \le r \le w/2)$:[62]

$$U(r) = -\left(\frac{2\pi\varepsilon_{Xe\text{–}C}n}{5}\right)\left[\frac{5(w/2a_{Xe\text{–}C} - r/a_{Xe\text{–}C})^6 - 2}{(w/2a_{Xe\text{–}C} - r/a_{Xe\text{–}C})^{10}} + \frac{5(w/2a_{Xe\text{–}C} + r/a_{Xe\text{–}C})^6 - 2}{(w/2a_{Xe\text{–}C} + r/a_{Xe\text{–}C})^{10}}\right], \quad (5)$$

where $\varepsilon_{Xe\text{–}C}$ is the depth of the potential well and $a_{Xe\text{–}C}$ is the average value of the LJ a-parameter for Xe–C pair. According to the Lorentz–Berthelot rule, $\varepsilon_{Xe\text{–}C}$ and $a_{Xe\text{–}C}$ are estimated from the LJ parameters for the Xe–Xe pair in gaseous xenon ($\varepsilon_{Xe\text{–}Xe}/k_B = 221\,K$ and $a_{Xe\text{–}Xe} = 0.410\,nm$)[63] and C–C pair of C atoms ($\varepsilon_{C\text{–}C}/k_B = 28\,K$ and $a_{C\text{–}C} = 0.34\,nm$)[63] as 78 K and 0.375 nm, respectively. The number of surface atoms in an area of $a^2_{Xe\text{–}C}$ is n. Assuming a graphite structure for the ACF micropore surface, we can readily infer that n is about three based on the hexagonal lattice parameter of graphite ($a = 0.2450\,nm$, $c = 0.6696\,nm$, $Z = 4$) and $a^2_{Xe\text{–}C}$. The dependence of δ_S on temperature and pore width is governed mainly by the potential surface between a xenon atom and all atoms comprising the wall surface. The equilibrium position of a xenon atom in the pore is characterized by a single minimum potential energy curve when the pore width is less than $2D_{Xe}$, where D_{Xe} is the van der Waals diameter of xenon. In this case, δ_S is proportional to temperature and depends little on the pore width. In contrast, when the pore width is greater than $2D_{Xe}$, the xenon–wall interaction is characterized by a double minimum potential, as described in Eq. 5, engendering the large temperature dependence of $\delta_S{}^{-1}$. In addition, the slope of $\delta_S{}^{-1}$ of the pore width is approximately proportional to the inverse of the potential depth of the xenon–wall interaction. The deeper potential depth causes a longer residence time of xenon near the ACF micropore surface, resulting in a shorter mean free path of xenon and larger chemical shift values. Cheung also presumed that $\delta(r)$ was proportional to the attractive part of the LJ potential, $\delta(r) = -4c\varepsilon[(a/r)^6]$. For a xenon atom trapped between two infinite parallel carbon sheets, summing up each contribution from the carbon atoms on the surface implies the following representation:[62]

$$\delta(r) = (2\pi\varepsilon_{Xe\text{–}C}nc)\left[\frac{1}{(w/2a_{Xe\text{–}C} - r/a_{Xe\text{–}C})^4} + \frac{1}{(w/2a_{Xe\text{–}C} + r/a_{Xe\text{–}C})^4}\right]. \quad (6)$$

Using Eqs. 5 and 6 for $U(r)$ and $\delta(r)$ in Eq. 4, the numerical integration of Eq. 4 from $-w/2$ to $w/2$ provides the δ_S value for the pore width w. We chose the constant c as an adjustable parameter to reproduce the dependence of $\delta_S{}^{-1}$ on pore width. The curve described by the solid line in Fig. 3 is obtained by $c = 0.046\,ppm\,K^{-1}$, which seems to reproduce the experimental values well.

This aspect demonstrates that the model proposed by Cheung describes the dependence of $\delta_S{}^{-1}$ on pore width in the ACF/Xe system; that is, our analysis implies that the dependence of $\delta_S{}^{-1}$ on pore width can be interpreted successfully in terms of the distribution of xenon based on the potential function characterizing the xenon–wall interaction. In fact, c has been derived theoretically by scaling the free atom shielding constant of xenon with the first ionization energies of xenon and carbon atoms, and estimated it as 0.127 ppm K^{-1}.[62,76] This value is about 2.7 times greater than the c value for reproduction of experimental data. This discrepancy is not surprising because the intermolecular shielding arises predominantly from the overlap and exchange of electrons. In this model, $\delta(r)$ includes only an attractive part of the LJ potential—the sixth order term of the inverse power of r. Therefore, $\delta(r)$ is too simple to describe the shielding surface between xenon and carbon layers. The higher order terms of the inverse power of r contribute effectively to $\delta(r)$. Currently, c is considered as a phenomenological parameter based on the crude approximation.

Density Dependence of ^{129}Xe Chemical Shifts in ACFs. The pressure dependence of the ^{129}Xe chemical shift value represented through δ_{Xe} results from xenon–xenon intermolecular interactions. Applying Henry's law to describe δ_{Xe}, the density of xenon in ACF micropores is inferred to be the same as that of bulk xenon. However, the fact that xenon adsorption is accelerated rapidly, even in the low-pressure region below 0.1 MPa, suggests that this assumption is not valid for the effective density of xenon in ACF micropores. Therefore, precise evaluation of the density dependence of the chemical shift, $\delta_{Xe\text{–}Xe}$, demands conversion of the pressure axis to a density axis using xenon adsorption isotherms on ACFs. Figure 4 shows the Xe adsorption isotherm for ACFs. The isotherms are typical I-type isotherms in IUPAC classification,[64,65] indicat-

ing that the micropore-filling mechanism accelerates xenon adsorption in the low-pressure region because of the emphasized potentials in nanospace. Similar behavior has been observed for supercritical gases such as He, N_2, and CH_4.[66] This adsorption isotherm has been well interpreted by the Dubinin–Radushkevich (DR) equation as:[58–60]

$$\left[\ln\left(\frac{W_0}{W_a}\right)\right]^{1/2} = \left(\frac{RT}{\beta E_0}\right)(\ln P_{eq} - \ln P), \quad (7)$$

where W_0 is the saturated amount of xenon, W_a is the adsorbed amount of xenon at pressure P, and P_{eq} is the quasi-saturated vapor pressure when the pore volume is filled completely with xenon. The effective adsorption potential energy of the micropore to xenon is represented as βE_0, where the β coefficient represents the degree of affinity between the wall and the adsorbate, and is 0.5 for xenon. In the DR relationship, βE_0 is associated with the isosteric heat of adsorption, q_{st}, using the enthalpy of vaporization ΔH_v (12.6 kJ mol^{-1}) at the boiling point of xenon as:[60,67]

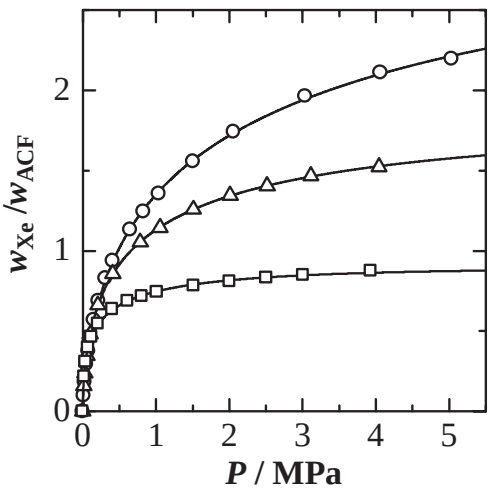

Fig. 4. Xenon adsorption isotherm for xenon adsorbed in ACF micropores at 298 K; 10A ($w = 0.7$ nm) (□), 15A ($w = 0.83$ nm) (△), and 20A ($w = 1.1$ nm) (○). The solid lines show the results of reproduction using Dubinin–Radushkevich (DR) equation.

$$q_{st} = \Delta H_v + \beta E_0, \quad (8)$$

where q_{st} is the heat of adsorption when the micropore is filled fractionally to $1/e$ of the total volume by adsorbates. In Fig. 4, the absolute amount of xenon adsorption is well reproduced by the Dubinin–Radushkevich (DR) equation; Table 3 lists the parameters using this reproduction. In this study, βE_0 and q_{st} were determined as somewhat larger (ca. 3 kJ mol^{-1}) than reported by Aoshima et al.,[60] but each parameter shows an identical trend of variation with respect to variations in pore width. The increase in pore width from 0.7–1.1 nm brings about a reduction of 1 kJ mol^{-1} (ca. 120 K) for the interaction between the wall and xenon. In addition, the quasi-saturated vapor pressure P_{eq} increases with increasing pore width. This concomitant increase reveals that narrow pores stabilize the xenon atoms, as expected, by the micropore-filling mechanism.

Division of the adsorption amount of xenon per gram of ACF by the micropore volume indicates the effective density of xenon in the ACF micropore to be 4.8×10^2 kg m^{-3} for 10A, 2.2×10^2 kg m^{-3} for 15A, and 1.0×10^2 kg m^{-3} for 20A at an equilibrium pressure of 0.01 MPa. These values are much larger than those of bulk xenon at 0.01 MPa ($\rho_{Xe} \approx 5 \times 10^{-1}$ kg m^{-3}) at 298 K. For that reason, it is expected that the plot of the chemical shift against the effective density of xenon exhibits a different slope from that against the density of bulk xenon gas, which corresponds to the K' value evaluated from Henry's law.

Next, we discuss the chemical shift as a function of the effective density of xenon adsorbed in the ACF micropore. Figures 5a–5c show δ plotted against the effective density of xenon in the micropores. As mentioned in the introduction, the dependence of δ on the effective density of xenon is ascrib-

Table 3. Saturated Amount of Xenon, W_0(Xe), Characteristic Adsorption Energy, βE_0, Isosteric Heat of Adsorption, q_{st}, and Quasi-Saturated Vapor Pressure, P_{eq}, of Supercritical Xenon Gas to ACF Micropores

Sample	W_0(Xe) (g/1 g ACF)	βE_0 /kJ mol^{-1}	q_{st} /kJ mol^{-1}	P_{eq} /MPa
10A	0.89 ± 0.05	13 ± 1	26.0 ± 1	9.3 ± 1
15A	1.76 ± 0.05	12 ± 1	24.6 ± 1	25 ± 3
20A	3.01 ± 0.05	12 ± 1	24.4 ± 1	70 ± 5

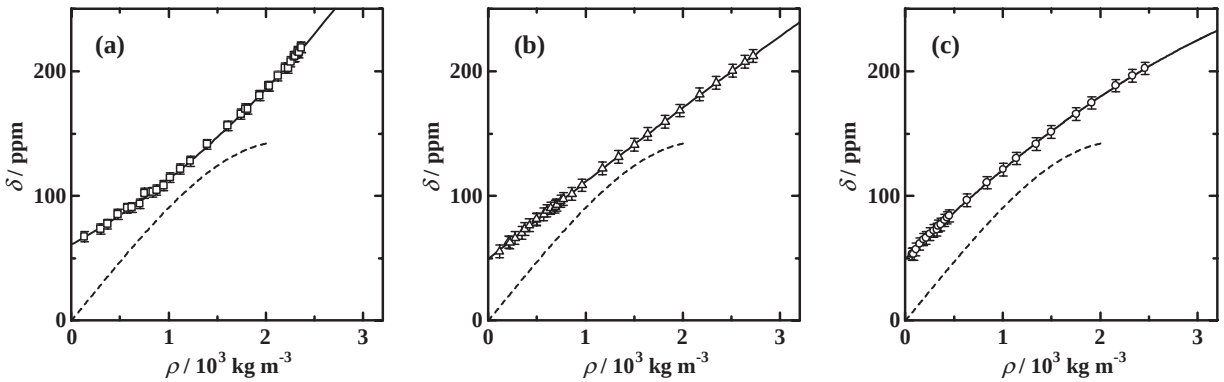

Fig. 5. The density dependence of δ_{Xe} for xenon confined in ACF micropores: 10A ($w = 0.7$ nm) (a), 15A ($w = 0.83$ nm) (b), and 20A ($w = 1.1$ nm) (c). The solid lines are the results of least-square fitting using Eq. 9. The dashed line shows the density dependence of the ^{129}Xe chemical shift of bulk xenon gas reported by Jameson et al.[29]

Table 4. Virial Coefficients of ^{129}Xe Chemical Shift for Bulk Xenon Gas and Confined Xenon in ACF Nanospace

Sample	δ_S /ppm	δ_1 $/10^{-3}$ ppm kg^{-1} m^3	δ_2 $/10^{-6}$ ppm (kg^{-1} m^3)^2	δ_3 $/10^{-9}$ ppm (kg^{-1} m^3)^3
10A	61 ± 4	42 ± 2	10 ± 1	—
15A	49 ± 5	63 ± 1	-1.2 ± 0.2	—
20A	49 ± 5	78 ± 1	-6.6 ± 0.4	—
Bulk	0.0	93.6	4.9	−8.1

ed mostly to the δ_{Xe} term in Eq. 1 in the low-density region. In bulk xenon gas, δ_{Xe} can be expanded by the xenon density as:[34]

$$\delta_{Xe} = \delta_0 + \delta_1\rho + \delta_2\rho^2 + \delta_3\rho^3 + \ldots . \quad (9)$$

Below 50 amagats (2.93×10^2 kg m^{-3}), which corresponds to about 5 MPa of ideal gas under standard conditions, the higher order terms that are higher than the quadratic term of density are negligible. Truncation well interprets the linear relationship of the density dependence of δ. Here, the coefficient δ_1 mainly reflects the xenon–xenon binary interatomic interaction, although the xenon–wall interaction also contributes a little to δ_1. On the other hand, in the high-pressure region where the density dependence of δ curves, the non-linear terms of the density contribute to the density dependence of δ. The non-linearity is represented by the virial coefficients of the third order and higher, which stem from the xenon–xenon ternary interatomic interaction as well as the xenon–wall interaction perturbed by the reduction of the free volume. In Figs. 5a–5c, δ exhibits the non-linear dependence on xenon density and the higher order terms that are higher than the quadratic term of density in Eq. 9 contribute efficiently in the density region of more than 1×10^3 kg m^{-3}. This equation is feasible to describe the change in δ by xenon density in ACF micropores. The density dependence of δ is therefore optimized by inserting Eq. 9, which includes up to the quadratic term of density, to the third term on the right-hand side of Eq. 1. Here, on the least square's analysis of the density dependence of δ using the virial expansion of the chemical shift, the truncation of the term higher than the cubic term leads to a virial coefficients with less uncertainty in comparison with the case of truncation higher than the fourth-order term. Table 4 lists the resultant virial coefficients, which affect xenon–xenon interaction in ACF micropores. The $|R|$ values for the non-linear least-square fitting were greater than 0.999 for all of the ACF samples. The resultant δ_S value was coincident with the δ_S' evaluated from Henry's law in 20A; for 10A and 15A it was 92% of δ_S'. That result suggests that with decreasing pore width, i.e., in the potential field caused by the micropore, the pressure dependence of δ overestimates δ_S' compared with true δ_S, based on the effective density of xenon in the micropores. On the other hand, the xenon–xenon interaction in the chemical shift is included in the virial coefficients. The second-virial coefficient, δ_1, was found to depend strongly on the pore width; δ_1 is the largest in bulk xenon and it decreases with decreasing pore width in ACF. This trend indicates the spatial size effect of xenon–xenon interactions in nanospace.

According to Jameson et al., δ_1 is given by the contribution of chemical shielding caused by the interatomic interaction between two xenon atoms. Although they used chemical shielding, σ, in their discussion, we use chemical shift representation, δ, for consistency of representation. Describing the shielding function between two xenon atoms by $\delta(r)$, which is a function of interatomic distance, δ_1 in bulk xenon is generally represented as[68]

$$\delta_1(T) = 4\pi \int_0^\infty \delta(r) r^2 \exp[-U(r)/kT]\mathrm{d}r, \quad (10)$$

where $U(r)$ is the pair potential between two xenon atoms. A series of the inverse power of r, $C_6r^{-6} + C_8r^{-8} + C_{10}r^{-10} + C_{12}r^{-12} + C_{14}r^{-14}$ can describe $\delta(r)$ approximately, according to Jameson et al.[69] Equation 10 means that δ_1 is given by integrating $\delta(r)$ over the space accessible by a xenon atom. Because the magnitude of the shielding $|\delta(r)|$ increases sharply with a decrease in the interatomic distance, the xenon atom occupying the space close to a given xenon atom, especially xenon atoms occupying the first coordination sphere, contribute dominantly to δ_1. In this case, Equation 10 will cause the largest absolute value in δ_1 because the infinite and isotropic space are taken into account by the integral. On the other hand, in micropores, the space contributing to the integral in Eq. 10 will be decreased by the hindrance of pore walls, expecting a smaller value in δ_1 than in bulk xenon. In ACF micropores, the δ_1 value is smaller than that of bulk xenon; it decreases from 78×10^{-3} to 42×10^{-3} ppm kg^{-1} m^3 with decreasing pore width from 1.1 nm in 20A to 0.7 nm in 10A, as shown in Fig. 6. Since δ_1 is concerned with the space around a given xenon atom for the integral, the ratio of δ_1 in

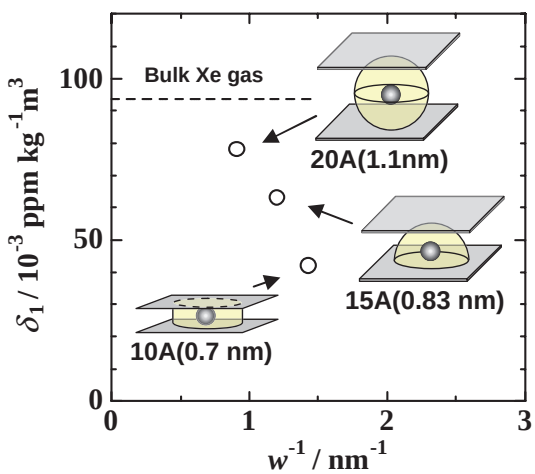

Fig. 6. Plot of δ_1 against the inverse of pore width, w^{-1}. δ_1 decreases with decreasing w. This variation reflects the first coordination sphere around a given xenon atom in each ACF micropore, which is evaluated to be 83, 67, and 45% of that in bulk xenon gas.

ACF to that of bulk xenon reflects the effective volume of the first coordination sphere in comparison with that of bulk xenon. The first coordination sphere is reduced to 83% for 20A, 67% for 15A, and 45% for 10A with respect to the first coordination sphere of bulk xenon gas.

Furthermore, the effective volume in the first coordination sphere involves decreasing the maximum coordination number of xenon confined in the ACF micropore, which might define the maximum size of the xenon cluster as the local structure. Formation of Xe_n clusters was confirmed using ^{129}Xe NMR in some zeolites such as NaA,[70,72,73] KA,[74] and AgA.[75] In the alpha-cage of A-type zeolites, the acceptable cluster size depends strongly on the void space accessible by xenon. Clusters up to $n = 8$ were observed in NaA[70] and AgA,[75] whereas clusters up to $n = 5$ were in KA.[74] For fast exchanging systems such as CaA,[71] the observed chemical shift can be interpreted by the weighted average of the inherent values of Xe_n clusters. In the ACF/Xe system, the local structure of xenon is well described by Xe_n clusters. The adsorption isotherm and the GCMC simulation study predicted formation of Xe_n clusters with $n = 1$–12 as the local structure of adsorbed xenon molecules.[43] Therefore, it is reasonable to consider that the observed signal in the ^{129}Xe NMR spectrum for the ACF/Xe system results from weighted averaging of the resonance peaks for xenon clusters under the fast exchange limit. The isotropic environment of bulk xenon gas assumes 12-coordination, which corresponds to a local structure of Xe_{13} cluster. Therefore, the maximum coordination number is reduced by the same ratio in the first coordination sphere: 10 for 20A, 8 for 15A, and 5.4 for 10A. These numbers are fundamentally related strongly to the maximum size of the Xe_n cluster formed in each ACF. The pore widths of 1.1 nm for 20A, 0.83 nm for 15A, and 0.7 nm for 10A correspond respectively to $2.5D_{Xe}$, $1.8D_{Xe}$, and $1.6D_{Xe}$. In contrast, assuming that xenon filling in the micropore occurs in the manner of closed-packing of xenon, the maximum cluster will be Xe_{13} for triple layer stacking in 20A, Xe_{10} for bilayer stacking in 15A, and Xe_7 for monolayer or incomplete bilayer stacking in 10A. These clusters require the free space of $2.6D_{Xe}$ for Xe_{13}, $1.8D_{Xe}$ for Xe_{10}, and $1.0D_{Xe}$ for Xe_7, and imply the maximum coordination numbers of 12, 9, and 6, respectively. These are somewhat larger than those resulting from δ_1. The large amplitude of molecular motion in gaseous xenon, like vibration and translation, actually causes a large excluded volume around a given xenon atom. Therefore, the number of xenon atoms accessible in the first coordination sphere is lower in ACF micropores. Considering the difference in the excluded volume between gaseous xenon and the closed-packed structure, the coordination number derived from δ_1 seems to be valid. Consequently, δ_1 is inferred to reflect the extension of the free space around a given xenon atom, which is closely related to the maximum coordination number of xenon in an ACF micropore. This aspect supports δ_1 as a useful index for the size effects on xenon–xenon intermolecular interactions in nanospace.

On the other hand, δ_2 and higher terms reflect the contribution of many-body intermolecular interactions among xenon atoms as well as between the adsorbed xenon atoms and the atoms that compose the pore wall. The value of δ_2 also depends on the pore width, implying that many-body interactions of xenon and xenon–wall interactions in the high-loading region are also affected by the acceptable space of other atoms around a xenon atom. The crowded environment around a xenon atom in the high-loading region induces the effective statistics of the interatomic interaction at short interatomic distances, resulting in a remarkable increase of the chemical shift in the high-loading region as observed in the 10A sample. The reduction of the free space that the adsorbed xenon atoms experience also brings about the effective statistics of the xenon–wall interatomic interactions at short interatomic distances. This effect will be mainly reflected on δ_2 as well. However, although the magnitude and the sign of δ_2 reflect interesting and important information regarding many-body intermolecular interactions, it is difficult to analyze and discuss these parameters because the theoretical background of δ_2 remains obscure.

Conclusion

The pressure dependence of ^{129}Xe chemical shift values adsorbed in slit-type ACF micropores was observed in the pressure region of 0.01–5 MPa by the in-situ high-pressure NMR method. The pressure dependence of the ^{129}Xe chemical shift value of xenon adsorbed in ACFs below 0.025 MPa obeys Henry's law, leading to the chemical shift value at zero pressure δ_S'. The dependence of δ_S' on ACF pore widths was well interpreted by a model proposed by Cheung. The xenon-adsorption isotherm was also measured, which enabled conversion of the pressure axis to the fluid density of xenon. The density dependence of ^{129}Xe chemical shift values was analyzed using the virial expansion of the chemical shift by xenon density. Subsequently, the virial coefficients were determined up to the second-order term on density. Results showed that the second-virial coefficient, δ_1, depends on the pore width. This variation in δ_1 was interpreted qualitatively in terms of the maximum size of Xe_n clusters as the local structure of xenon adsorbed in the ACF nanospace. This aspect suggests that the void space strongly affects xenon–xenon interactions in nanospace (spatial size effect on the intermolecular interaction). Thus, high-pressure ^{129}Xe NMR sheds light on new porosimetry to elucidate xenon-adsorption behavior and to quantitatively examine the interactions between pores and xenon atoms in porous materials.

The authors acknowledge Grants-in-Aid for Scientific Research (No. 11440176 and No. 16550013) from the Japanese Ministry of Education, Culture, Sports, Science and Technology.

References

1 P. J. Barrie, J. Klinowski, *Prog. Nucl. Magn. Reson. Spectrosc.* **1992**, *24*, 91, and references therein.

2 D. Raftery, B. F. Chmelka, *NMR Basic Principles and Progress*, **1994**, Vol. 30, p. 112, and references therein.

3 J. Fraissard, *Encyclopedia of Nuclear Magnetic Resonance*, ed. by M. Grant, R. Harris, John Wiley & Sons, Chichester, **1996**, Vol. 5, p. 3058.

4 C. I. Ratcliffe, *Annu. Rep. NMR Spectrosc.* **1998**, *36*, 124, and references therein.

5 M.-A. Springuel-Huet, J.-L. Bonardet, A. Gédéon, J.

Fraissard, *Magn. Reson. Chem.* **1999**, *37*, S1, and references therein.
6 T. Ito, J. Fraissard, in *Proceedings of the 5th International Zeolite Conference*, ed. by L. V. C. Ree, Heyden, London, **1980**, p. 510.
7 J. A. Ripmeester, D. W. Davidson, *J. Mol. Struct.* **1981**, *75*, 67.
8 A. C. de Dios, C. J. Jameson, *Annu. Rep. NMR Spectrosc.* **1994**, *29*, 1.
9 I. L. Moudrakovski, A. Sanchez, C. I. Ratcliffe, J. A. Ripmeester, *J. Phys. Chem. B* **2000**, *104*, 7306.
10 M. S. Syamala, R. J. Cross, M. Saunders, *J. Am. Chem. Soc.* **2002**, *124*, 6216.
11 J. M. Kneller, R. J. Soto, S. E. Surber, J.-F. Colomer, A. Fonseca, J. B. Nagy, G. V. Tendeloo, T. Pietrass, *J. Am. Chem. Soc.* **2000**, *122*, 10591.
12 A. P. M. Kentgens, H. A. van Boxtel, R.-J. Verweel, W. S. Veeman, *Macromolecules* **1991**, *24*, 3712.
13 M. Tomaselli, B. H. Meier, P. Robyr, U. W. Suter, R. R. Ernst, *Chem. Phys. Lett.* **1993**, *205*, 145.
14 K. Sperling-Ischinsky, W. S. Veeman, *J. Braz. Chem. Soc.* **1999**, *10*, 299.
15 B. Nagasaka, H. Omi, T. Eguchi, H. Nakayama, N. Nakamura, *Chem. Phys. Lett.* **2001**, *340*, 473.
16 J. A. Ripmeester, C. I. Ratcliffe, J. S. Tse, *J. Chem. Soc., Faraday Trans. 1* **1988**, *84*, 3731.
17 J. A. Ripmeester, C. I. Ratcliffe, *J. Phys. Chem.* **1990**, *94*, 8773.
18 I. L. Moudrakovski, A. A. Sanchez, C. I. Ratcliffe, J. A. Ripmeester, *J. Phys. Chem. B* **2001**, *105*, 12338.
19 V. J. Storhaug, F. Liebig, C. R. Bowers, *J. Phys. Chem. B* **2002**, *106*, 2884.
20 O. Muenster, J. Jokisaari, P. Diehl, *Mol. Cryst. Liq. Cryst.* **1991**, *206*, 179.
21 J. Bharatam, C. R. Bowers, *J. Phys. Chem. B* **1999**, *103*, 2510.
22 M. Ylihautala, J. Lounila, J. Jokisaari, *Chem. Phys. Lett.* **1999**, *301*, 153.
23 A. Cherubini, A. Bifone, *Prog. Nucl. Magn. Reson. Spectrosc.* **2003**, *42*, 1, and references therein.
24 E. Locci, Y. Dehouck, M. Casu, G. Saba, A. Lai, M. Luhumer, J. Reisse, K. Bartik, *J. Magn. Reson.* **2001**, *150*, 167.
25 S. M. Rubin, M. M. Spence, A. Pines, D. E. Wemmer, *J. Magn. Reson.* **2001**, *152*, 79.
26 Q. J. Chen, J. Fraissard, *J. Phys. Chem.* **1988**, *96*, 5170.
27 J. Demarquay, J. Fraissard, *Chem. Phys. Lett.* **1987**, *136*, 314.
28 T. Ueda, T. Eguchi, N. Nakamura, R. E. Wasylishen, *J. Phys. Chem. B* **2003**, *107*, 180.
29 A. K. Jameson, C. J. Jameson, H. S. Gutowsky, *J. Chem. Phys.* **1970**, *53*, 2310.
30 C. J. Jameson, A. C. de Dios, *J. Chem. Phys.* **2002**, *116*, 3805.
31 C. J. Jameson, *J. Chem. Phys.* **2002**, *116*, 8912.
32 B. Nagasaka, T. Eguchi, H. Nakayama, N. Nakamura, Y. Ito, *Radiat. Phys. Chem.* **2000**, *58*, 581.
33 H. Kobayashi, T. Ueda, K. Miyakubo, T. Eguchi, *Z. Naturforsch., A: Phys. Sci.* **2003**, *58*, 727.
34 H. Omi, B. Nagasaka, K. Miyakubo, T. Ueda, T. Eguchi, *Phys. Chem. Chem. Phys.* **2004**, *6*, 1299.
35 N. Kato, T. Ueda, H. Omi, K. Miyakubo, T. Eguchi, *Phys. Chem. Chem. Phys.* **2004**, *6*, 5427.
36 D. Baumer, A. Fink, E. Brunner, *Z. Phys. Chem.* **2003**, *217*, 289.
37 K. Kaneko, C. Ishii, M. Ruike, H. Kuwabara, *Carbon* **1992**, *30*, 1075.
38 K. Kaneko, C. Ishii, N. Nagi, Y. Hanazawa, N. Setoyama, T. Suzuki, *Adv. Colloid Sci.* **1998**, *76*, 295.
39 K. Kaneko, *Supramol. Sci.* **1998**, *5*, 267.
40 N. Setoyama, K. Kaneko, *Adsorption* **1995**, *1*, 165.
41 N. Setoyama, K. Kaneko, F. Rodroguez-Reinozo, *J. Phys. Chem.* **1996**, *100*, 10331.
42 D. Nemirovsky, R. Moreh, K. H. Andersen, J. Mayers, *J. Phys.: Condens. Matter* **1999**, *11*, 6653.
43 M. Aoshima, T. Suzuki, K. Kaneko, *Chem. Phys. Lett.* **1999**, *310*, 1.
44 Z. M. Wang, T. Suzuki, N. Uekawa, K. Asakura, K. Kaneko, *J. Phys. Chem.* **1992**, *96*, 10917.
45 T. Iiyama, K. Nishikawa, T. Otowa, T. Suzuki, K. Kaneko, *J. Phys. Chem.* **1995**, *99*, 10075.
46 T. Iiyama, K. Nishikawa, T. Suzuki, K. Kaneko, *Chem. Phys. Lett.* **1997**, *274*, 152.
47 C. Pelekani, V. L. Snoeyink, *Water Res.* **1999**, *33*, 1209.
48 T. Ohkubo, T. Iiyama, K. Nishikawa, T. Suzuki, K. Kaneko, *J. Phys. Chem.* **1999**, *103*, 1859.
49 T. Iiyama, K. Nishikawa, T. Suzuki, T. Otowa, M. Hijiriyama, Y. Nojima, K. Kaneko, *J. Phys. Chem.* **1997**, *101*, 3037.
50 T. Suzuki, K. Kaneko, K. E. Gubbins, *Langmuir* **1997**, *13*, 2545.
51 A. Watanabe, T. Iiyama, K. Kaneko, *Chem. Phys. Lett.* **1999**, *305*, 71.
52 K. Kaneko, K. Yamaguchi, C. Ishii, S. Ozeki, S. Hagiwara, T. Suzuki, *Chem. Phys. Lett.* **1991**, *176*, 75.
53 H. Kanoh, K. Kaneko, *J. Phys. Chem.* **1995**, *99*, 5746.
54 H. Kanoh, A. Zamma, N. Setoyama, Y. Hanzawa, K. Kaneko, *Langmuir* **1997**, *13*, 1047.
55 Z. M. Wang, K. Kaneko, *J. Phys. Chem.* **1995**, *99*, 16714.
56 N. Setoyama, T. Suzuki, K. Kaneko, *Carbon* **1998**, *36*, 1459.
57 E. A. Ustinov, D. D. Do, A. Herbst, R. Staudt, P. Harting, *J. Colloid Interface Sci.* **2002**, *250*, 49.
58 M. M. Dubinin, *Chem. Rev.* **1960**, *60*, 235.
59 S. G. Chen, R. T. Yang, *Langmuir* **1994**, *10*, 4244.
60 M. Aoshima, K. Fukasawa, K. Kaneko, *J. Colloid Interface Sci.* **2000**, *222*, 179.
61 A. Nakayama, C. Ishii, T. Takayama, M. Watanabe, A. Zanma, K. Kaneko, K. Sugihara, *Synth. Met.* **1997**, *86*, 2335.
62 T. T. P. Cheung, *J. Phys. Chem.* **1995**, *99*, 7089.
63 G. Stan, M. J. Bojan, S. Curtarolo, S. M. Gatica, M. W. Cole, *Phys. Rev. B* **2000**, *62*, 2173.
64 K. S. W. Sing, D. H. Everett, R. A. W. Haul, L. Moscou, R. A. Pierotti, *Pure Appl. Chem.* **1985**, *57*, 603.
65 K. Kaneko, *J. Membr. Sci.* **1994**, *96*, 59.
66 K. Kaneko, K. Shimizu, T. Suzuki, *J. Chem. Phys.* **1992**, *97*, 8705.
67 B. P. Bering, M. M. Dubinin, V. V. Serpinsky, *J. Colloid Interface Sci.* **1966**, *21*, 378.
68 C. J. Jameson, A. K. Jameson, S. M. Cohen, *J. Chem. Phys.* **1973**, *59*, 4540.
69 C. J. Jameson, D. N. Sears, A. C. de Dios, *J. Chem. Phys.* **2003**, *118*, 2575.
70 C. J. Jameson, A. K. Jameson, R. Gerald, II, A. C. de Dios, *J. Chem. Phys.* **1992**, *96*, 1676.

71 C. J. Jameson, A. K. Jameson, R. Gerald, II, A. C. de Dios, *J. Chem. Phys.* **1992**, *96*, 1690.
72 C. J. Jameson, A. K. Jameson, B. I. Baello, H.-M. Lim, *J. Chem. Phys.* **1994**, *100*, 5965.
73 C. J. Jameson, A. K. Jameson, H.-M. Lim, B. I. Baello, *J. Chem. Phys.* **1994**, *100*, 5977.
74 C. J. Jameson, A. K. Jameson, R. Gerald, II, H.-M. Lim, *J. Chem. Phys.* **1995**, *103*, 8811.
75 I. L. Moudrakovski, C. I. Ratcliffe, J. A. Ripmeester, *J. Am. Chem. Soc.* **1998**, *120*, 3123.
76 R. A. Kromhout, B. J. Linder, *J. Magn. Reson.* **1969**, *1*, 450.
77 H. Omi, T. Ueda, K. Miyakubo, T. Eguchi, *Appl. Surf. Sci.* **2005**, *252*, 660.
78 C. R. Yonker, S. L. Fry, D. R. Kalkwarf, R. D. Smith, *J. Phys. Chem.* **1986**, *90*, 3022.
79 D. M. Pfund, T. S. Zemanian, J. C. Linehan, J. L. Fulton, C. R. Yonker, *J. Phys. Chem.* **1994**, *98*, 11846.
80 D. G. Moses, F. G. Baglin, *J. Phys. Chem.* **1987**, *91*, 1942.
81 J. Jonas, *NMR Basic Principles and Progress*, Springer-Verlag, Berlin, **1991**, Vol. 24.
82 M. Poliskoff, S. M. Howdle, S. G. Kazarian, *Angew. Chem., Int. Ed. Engl.* **1995**, *34*, 1275.
83 G. Kaupp, *Angew. Chem., Int. Ed. Engl.* **1994**, *33*, 1452.
84 P. G. Jessop, Y. Hsiao, T. Ikariya, R. Noyori, *J. Am. Chem. Soc.* **1996**, *118*, 344.